Characteristics of the Hubble Space Telescope's Radiation Environment Inferred From Charge–Collection Modeling of Near-Infrared Camera and Multi-Object Spectrometer Darkframes

R. Ladbury, *Member, IEEE*, J. C. Pickel, *Member, IEEE*, G. Gee, *Member, IEEE*, Tom M. Jordan, *Member, IEEE*, L. Bergeron, B. Rauscher, Robert A. Reed, *Member, IEEE*, Paul W. Marshall, *Member, IEEE*, D. Figer, B. Fodness, *Member, IEEE*, and S. Kniffin, *Member, IEEE*

Abstract—Dark frames from orbiting infrared detector arrays are analyzed using a charge–collection model to investigate the effects of secondary and primary particle environments in infrared detectors and related electronics. The effects of different components of the primary and secondary environments are assessed by examining trends with time and pixel-to-pixel charge correlations.

I. INTRODUCTION

USE OF sensitive infrared detectors in space poses significant challenges for the astronomy, military, and radiation-effects communities. These devices are designed to respond to the low levels of ionization deposited by infrared photons. This high detector sensitivity, coupled with the faintness of infrared sources typically observed by these detectors, necessitates that detectors operate at cryogenic temperatures, where charge mobilities are low and charges can become metastably trapped. As such, infrared detectors are susceptible to a rich variety of radiation effects that can be caused not just by proton-induced nuclear recoils and heavy ions but also by single low-LET (so-called minimum-ionizing) particles in the radiation environment [1]–[3]. Moreover, the faintness of most infrared sources of interest means that observations are often of long duration so there is ample opportunity for radiation effects to corrupt detector readings.

Previous studies have reported significantly higher-than-expected rates of radiation-induced contamination in images and have suggested that the discrepancy could be due to particles created by interactions between the primary radiation environment and spacecraft structures [4], [5]. This "secondary radiation environment" has not traditionally been modeled down to the level of single-particle effects. This is partly because higher LET particles in the primary environment and recoils from proton-induced nuclear interactions generally dominate single-event rates for most electronics applications. Also, the dependence of the secondary radiation environment on spacecraft structures means that it will be unique to each spacecraft. In addition, while some of these terms, such as bremsstrahlung-photon and delta-ray production, take place promptly with the passage of the primary particle, others such as radioactivation and phosphorescence depend on spacecraft and detector composition and decay over time following an initial high radiation exposure. Moreover, even primary radiation events can have prolonged consequences. Because of their cryogenic operating temperatures, charges generated by a radiation exposure (or a bright infrared source) can become metastably trapped, increasing dark currents for struck pixels during subsequent observations. In subsequent images, this "persistence" imposes a faint afterglow of the initial event. The glow grows fainter as the charge decays exponentially with time. Persistence can also affect detector calibration since it will be indistinguishable from dark current over short timescales. Despite these difficulties, the advantages to be gained from space-based use of IR detectors make the development and calibration of tools for modeling radiation effects therein increasingly important.

The so-called "dark-frame" images from the Hubble Space Telescope's (HST) near-infrared camera and multi-object spectrometer (NICMOS) represent a potentially rich source of data for understanding the components of the radiation environment (primary and secondary) that are significant for infrared detectors. These dark frames were taken with the instrument filter wheel closed, so pixel readings substantially above background are largely due to the passage of ionizing radiation through the detectors and associated electronics [6].

The current study examines these data using a simplified charge–collection model to draw conclusions about both the radiation environment and the detectors' responses to it [7].
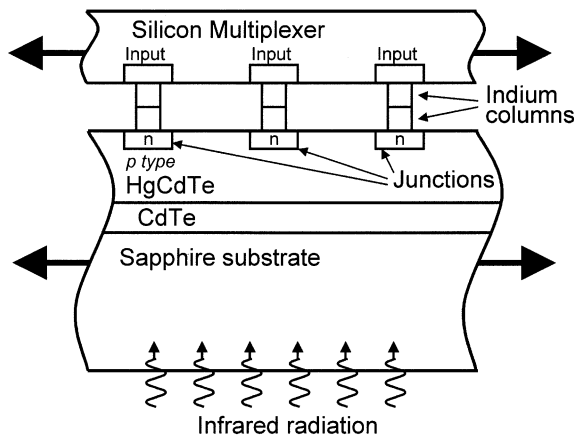
Fig. 1. NICMOS detectors consist of a HgCdTe active area beneath a CdTe dead layer (opaque to visible light) bonded to an Al_2O_3 substrate. Individual pixels are read out by an Si multiplexer with charge conducted via indium columns.

NICMOS Unit Cell

Fig. 2. The NICMOS unit cell consists of the detector (HgCdTe active region and associated storage element) and various access and reset FETs.

Fig. 3. Typical NICMOS darkframe image shows evidence of cosmic rays (bright spots) on an otherwise dark field of view.

II. OVERVIEW OF THE ANALYSIS

A. Detector Technology

The 40-μm pitch photovoltaic detectors used on NICMOS are fabricated in HgCdTe. The band structure of the ternary semiconductor $Hg_xCd_{(1-x)}Te$ can be adjusted by varying the relative proportions of Hg (x) and Cd ($1 - x$). For the NICMOS detectors $x \approx 0.3$, and it takes about 1 eV to produce an electron–hole pair; a relation that makes it possible to express $-dE/dx$ either in eV/μm or electrons per micron. A similar equivalence is possible for LET.

In normal operation (see Fig. 1), infrared light is incident on the detector through the sapphire and CdTe substrates. As the light passes through the detector material, it generates charge. Because of the long integration times typical for infrared detectors, all the charge is either collected (by drift or diffusion) or recombines. At the end of the integration, the multiplexer reads out the charge on each detector pixel via its access FET.

Ionization generated by charged particles that strike the detector pixel will be similarly collected and will contaminate subsequent pixel readings. Generally, a charged particle strike will produce a large discontinuous change in the charge on a pixel. Such a rapid rise is often distinguishable from the gradual rise expected when viewing faint infrared sources. Thus, it is often possible to use cosmic ray rejection algorithms to distinguish radiation-contaminated from uncontaminated pixels. So it is not just the absolute number of background events that contaminate pixel readings, but also their distribution with deposited charge that is important.

B. NICMOS and NICMOS Dark Frames

Placed in service during the second HST servicing mission in February 1997, NICMOS serves as a polarimeter, spectrometer, coronagraph, and photometer in the spectral range from 0.8 to 2.5 μm. The instrument includes three cameras equipped with 256×256 pixel HgCdTe photovoltaic detectors [8]. The array typically operates in the temperature range of 77–85 K.

The majority of NICMOS's radiation exposure comes from high-energy protons that strike the instrument when HST's orbit
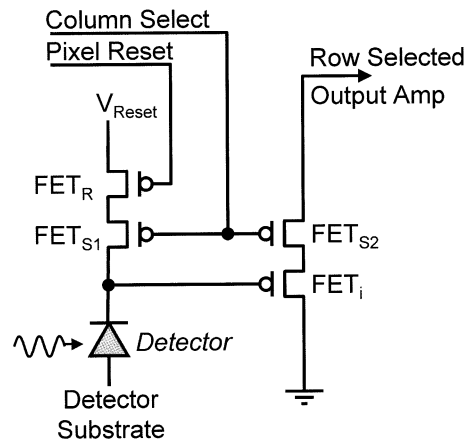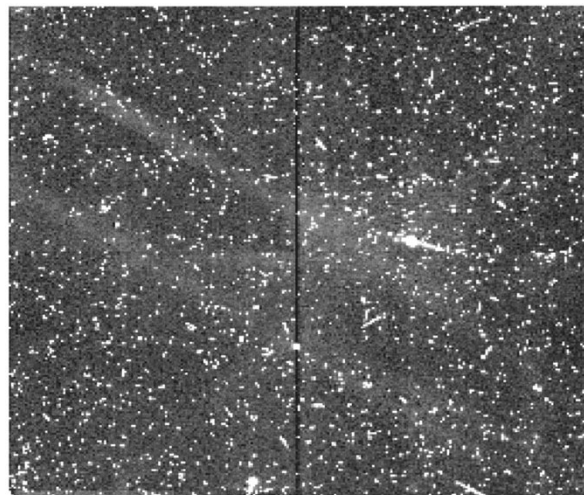
(90 min, 596 km $\times$ 619 km at $28°$ inclination) traverses some portion of the South Atlantic Anomaly (SAA) (about nine times per day). Operational constraints preclude operation of HST during SAA traverses, where proton hit rates range from about ten to a few thousand per square centimeter per second [9]. Outside the SAA, incident particles are predominantly Multi-GeV galactic cosmic ray (GCR) protons, which strike the array only about once in 7s.

The NICMOS dark frame data were gathered to measure detector dark currents and to calibrate cosmic-ray rejection algorithms [10]. Typically, each dark frame dataset consists of a series of images, including a reference image taken 0.203 s after array activation, followed by multiple images sampling the integral pixel contents at preset intervals. Each frame also contains information about sample timing, errors and data quality (see Fig. 3.)

Table I lists the dates and positions of HST when the dark frames used in this analysis were recorded. The last column gives the time the from the last SAA passage to the beginning of the dark frame and the time HST spent in the SAA during that passage.

TABLE I
DATES AND POSITIONS OF HST

Date	Position/ Altitude	Time Since and Duration in Last SAA pass
3/25/98	120° W, 28° N, 616 km	35 minutes, 20 minutes
4/23/98	119° E, 11° N, 614 km	6 minutes, 15 minutes
5/20/98	74° E, 14° N, 601 km	38 minutes, 10 minutes
7/16/98	56° E, 8° W, 598 km	6 minutes, 7 minutes
8/12/98	38° E, 6° N, 604 km	355 minutes, 10 minutes

TABLE II
FLUXES IMPLIED BY AVERAGE EVENT RATES

Hit size (# of electrons)	Flux (#/cm^2-s)	Probable causes
8000-15000	0.174	GCR protons, secondary electrons
15000-35000	0.119	Low-energy particles, low-angle GCR protons
>35000	0.03	mainly low-energy protons and alphas

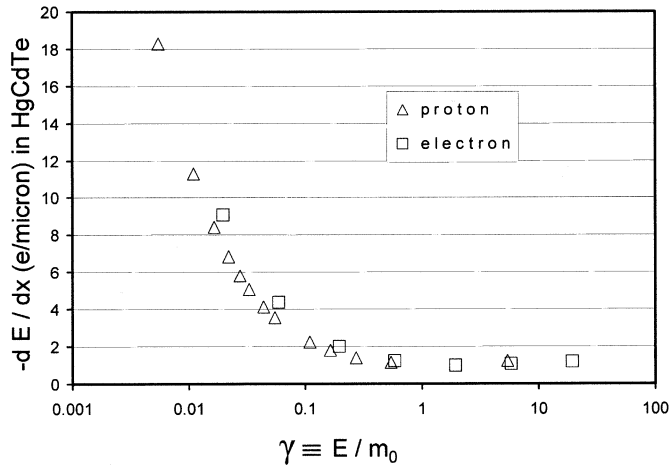Fig. 4. A plot of $-dE/dx$ versus γ, the ratio of a particle's energy E to its rest mass m_0, shows that as $\gamma \to 1$, $-dE/dx$ approaches a minimum.

C. Model of Detector Charge Collection

Because of the higher density and lower electron–hole pair production threshold in HgCdTe relative to Si, charged particles passing through the former generate nearly $10\times$ as much charge per unit track length as in the latter. For this reason, the charge–collection model used in these analyses assumes that charge collection in the detectors predominates over that in the corresponding multiplexer [7]. The charge–collection volumes in the detector and multiplexer are defined by their respective geometries and/or minority carrier diffusion lengths. Charge–collection efficiency in depletion regions was assumed to be 100%. Charge collection in the diffusion region was modeled using a three-dimensional diffusion equation [11]. Typically, the model produced a charge–collection efficiency in the diffusion region of about 50%.

The primary radiation environment was modeled as consisting mainly of high-energy protons and heavy ions using the CREME96 model. Outside the SAA, the vast majority of incident particles are minimum-ionizing, multi-GeV galactic cosmic ray protons, for which LET varies only slightly with energy (around 1.2 keV/μm in HgCdTe and less than half that in Si). LET rises considerably for protons with lower energies. (See Fig. 4.) LET values for electrons with energies higher than about 300 keV are comparable to those of high energy protons. Effectively, protons with energies greater than 600 MeV and

electrons with energies greater than about 300 keV ($\gamma \equiv E/m_0$ approaching 1) are minimum ionizing. That is, regardless of the particle type, the charge deposited in a given pixel depends almost exclusively on the path the particle takes through the pixel. The model used here assumes that protons follow straight-line trajectories. Trajectories of secondary electrons, which may scatter a great deal because of their small mass and relatively low energy, were modeled using the NOVICE Monte Carlo transport code [12]. Note that the multiple scattering undergone by an electron means that it will deposit somewhat more charge on average than a proton.

Assuming that the pixel charge collection volume is a rectangular parallelepiped with a 10-μm diffusion length and a 40-μm pitch, the average straight-line path length would be about 13.3 μms, implying a peak in the hit-size distribution at about 8000 electrons for the charge–collection model used here. There would also be substantial numbers of pixels with 8000–15 000 electrons. The maximum path length through such a pixel would be 57.5 μm. This implies that hit sizes greater than about 35 000 electrons would have to be due to intermediate-energy (0.1–0.5 GeV) protons or high-energy, minimum-ionizing light ions (mainly alpha particles). Lower hit sizes would arise predominantly from particles passing along short pathlengths through multiple pixels, from charge sharing (via diffusion) between a struck pixel and its nearest neighbors and from very low energy, range-limited particles (presumably electrons). Secondary photons (mainly bremsstrahlung radiation) are generally too weakly interacting to contribute significant charge to the detector array.

III. DATA PROCESSING

Differential images were constructed from the integral images by subtracting each image from the one succeeding it. Hot (high dark current) and cold (unresponsive) pixels were removed from the dataset. Finally, estimates of dark current and pedestal noise in the pixels were subtracted. The resulting frames were clean until radiation events began to affect the pixels.

Initial analysis of these differential images focused on hits with relatively simple geometries. These were selected by finding frames where readings for individual pixels increased substantially from one image to the next. To determine a typical hit topology, multiple hits were "stacked" or averaged. This resulted in cross-shaped topologies with electron counts in the struck pixel from around 10 000, and counts up to a few percent of the struck-pixel electron count in the four nearest-neighbor pixels (see Fig. 5.) As can be understood in
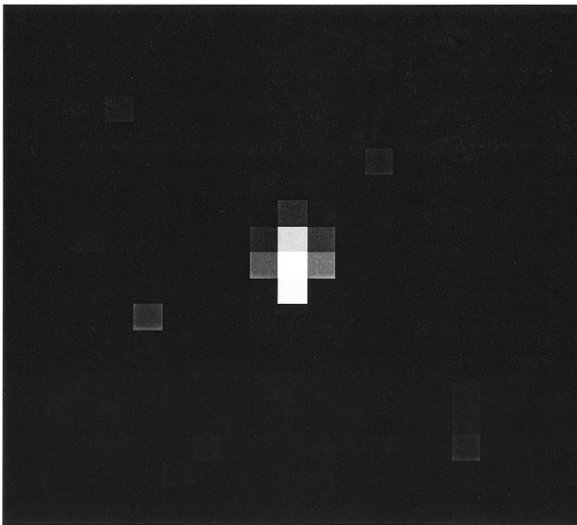
Fig. 5. Stacking of multiple hits results in an average, cross-shaped hit topology with nearest neighbors sharing a few percent of the charge in the struck pixel and diagonal neighbors sharing somewhat less.
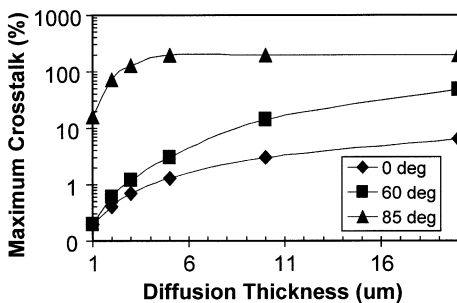

Fig. 6. Crosstalk between neighboring pixels arises from diffusion and is typically a few percent, depending on the diffusion layer thickness. For particles incident at grazing incidence, crosstalk can be much larger.
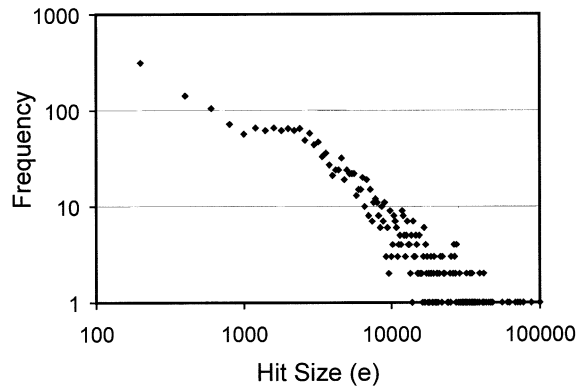

Fig. 7. Frequency distribution of hit sizes generated over six sequential 256-s darkframes.
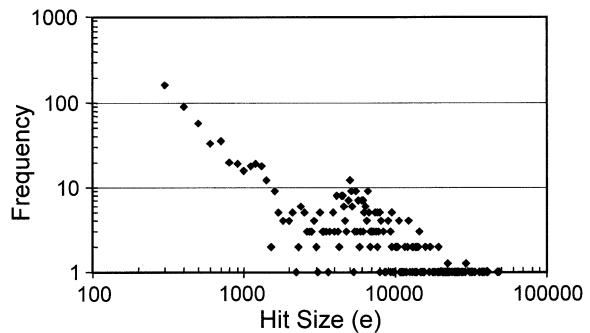
Fig. 8. A simulated frequency distribution of hit size generated assuming the model of [7].

terms of the charge collection model discussed earlier (and described in more detail in [7]), this charge spreading from the struck pixel to adjacent pixels occurs by diffusion and depends strongly on diffusion-layer thickness. Typically, the amount of charge shared by nearest neighbors was about 1% of the charge collected in the struck pixel (see Fig. 6), consistent with a diffusion depth of 5–10 μm. Hits incident at steeper angles resulted in much higher levels of charge sharing.

Because it is not possible to obtain noise-free data, the numbers of hits and the numbers of pixels affected by a hit depended on the value of the threshold selected. We chose a threshold of about 200 electrons, because the event counts and sizes became relatively stable above this level. Given that the read noise in NICMOS is typically 30 electrons and that the charge–collection model indicates that protons and other high-energy charged particles would typically deposit a few thousand electrons per pixel, we are confident that this threshold requirement excludes most random fluctuations in the array while missing few radiation events.

Hits with more complicated geometries (affecting multiple pixels) were found by selecting pixels with high counts and including all contiguous cells with counts above a given threshold. We also observed that even for events with more

complex topologies, the levels of charge spreading seen in adjacent pixels averaged on the order of a few percent, indicating that diffusion accounts for the charge levels in neighbor pixels for these events as well. Depending on the path and LET of the particle through the array, the numbers of pixels affected varied from 1 to greater than 100 pixels.

For each hit in which the struck pixel had greater than 200 electrons, we examined the behavior of the struck pixel in prior frames of the dataset (to look for persistence). Pixels that showed evidence of persistence (not more than 30 pixels per frame) were excluded from the analysis. We also recorded the contents of up to 120 pixels surrounding the struck pixel to investigate hit geometry and charge sharing among pixels.

IV. DISCUSSION

A. Hit Frequencies and Hit Sizes

An important question in light of the higher-than expected transient rate observed by the Infrared Space Observatory (ISO) is how frequently NICMOS cameras were struck by contaminating radiation, that is, the hit frequency. However, as mentioned above, the sizes of the hits are also important, since large hits can often be identified and rejected. The frequency distribution of hit sizes accumulating during several sequential 256-s frames shows that small hits dominate (see Fig. 7). As discussed earlier, this can be understood from the fact that a single hit usually affects several pixels, either by passing through them directly or via charge diffusion. Fig. 8 shows a simulated distribution of hits generated assuming the model of [7]. As can be seen by comparing the simulated and real hit distributions, the agreement is good at low hit size (pixel electron count) at least
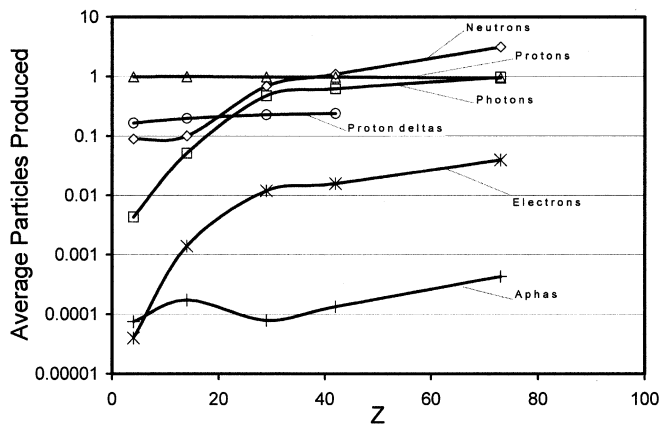
Fig. 9. Secondary particles produced per GCR proton. Delta rays predominate the secondary ionizing radiation spectrum.

qualitatively. For hit sizes corresponding to those expected from typical, multi-GeV GCR protons (8000–35 000 electrons, with the majority lying in the 8000–15 000 electron range), the current analysis indicates about 0.23 hits per camera per second. This corresponds to an implied particle flux of 0.293 hits/cm^2-s compared to the mean GCR rate of 0.175 protons/cm^2-s.

However, studies of secondary-particle production using the NOVICE Monte Carlo code indicate that nearly half of the difference may be explained by secondary particle production. These studies indicate that delta rays are the predominant ionizing secondary particle produced by interactions of protons with spacecraft structures. (See Fig. 9.) In addition, an analysis of hits in this range shows that 50% of them are associated with a nearby or adjacent hit of comparable magnitude ($>$8000 electrons). Thus, it appears that the portion of the excess that cannot be accounted for by delta ray production may be attributable to sharing of charge between pixels—perhaps an indication that further optimization is possible for the diffusion model.

We also note that over this range, there is no consistent trend in the data with time since the last SAA passage or with the duration of the most recent passage. This suggests that short-lived radionuclides activated by space radiation contribute negligibly to the contamination of NICMOS pixels during the timescales of these measurements ($<$1 year of radiation exposure, $<$30 min per SAA pass, and $\sim$30 min since the last SAA pass).

A potentially more significant difference between the NICMOS data and the simulation is seen in the intermediate electron-count range, from about 1500–5000 electrons. Here, the NICMOS data exceeds the predicted distribution by a factor of 5 or more. Again, no consistent trend is seen with time, indicating that radioactivation is not an explanation. In addition, the low levels of ionization indicated by these charge levels suggest either a weakly ionizing radiation source (50% that of a singly charged minimum-ionizing particle in HgCdTe) or higher LET sources with extremely short ranges in detector materials. If one assumes that these events arise from a weakly ionizing source term, and also that the mean path-length through the detector region is 13.3 μm (as assumed throughout the forgoing analysis), then the ionizing radiation produces 100–350 electrons per micron. This corresponds to values for $-dE/dx$ of 100–350 eV/μm in HgCdTe or

300–1300 eV/μm in Si. We note that the range for Si would not preclude high-energy protons and electrons. This may suggest that despite the lower charge yield, it is necessary to consider hits to the Si multiplexer as well as the HgCdTe detector. This explanation implies a significant number of strikes to the Si multiplexer not associated with hits to the corresponding HgCdTe detector pixel.

On the other hand, if one assumes that the intermediate electron counts result from particles with very limited range, it is clear that such particles must be incident on the sensitive regions of the detector from the direction of the multiplexer, since they would not have sufficient range to penetrate the Al_2O_3/CdTe substrate above the active region of the detector.

An alternative explanation may be that parameters of the current model need to be optimized for NICMOS detectors. That is, parameters such as the detector geometry or diffusion layer thickness may need to be changed to obtain adequate agreement. These changes would have to be subtle to preserve the generally good agreement seen at the low-LET and high-LET ends of the spectrum.

B. Persistence

Although the discussion to this point has not focused on persistence in IR detectors, it is an important fact of life for operation at cryogenic temperatures. At a minimum, understanding persistence is necessary in order to keep it from contaminating studies of detector radiation response. As such, the current analysis rejects pixels that exhibited evidence of persistence. According to the *NICMOS Instrument Handbook for Cycle 11* [8], pixels exposed to a source of ionizing radiation (be it infrared radiation, high-energy protons, etc.) that produces more than 130 000 electrons will tend to exhibit persistence. Because protons in the SAA typically have lower energies and are more heavily ionizing than GCR protons, they often produce signals of this magnitude, making persistence common after SAA passages. The resulting increased dark current decays exponentially, with a time constant on the order of 6 min.

For the current analysis, we rejected any pixel that had a count of more than 200 electrons in any prior frame. This allowed us to exclude most of the pixels that exhibited persistence while having only a 4% chance of excluding valid data from the study.

C. Implications for Space Applications

As mentioned earlier, the ease with which radiation-induced contamination can be detected and rejected during an observation varies inversely with the charge contamination deposited in the pixel. Large jumps arising from the passage of a cosmic ray bear little resemblance to the relatively gradual increases in collected charge typical of faint infrared sources. As such, the typical proton hit often represents more of a nuisance than a threat to data quality. Of greater concern are the fainter sources of ionization, particularly if they cannot be properly modeled. Given the increasing sensitivity of infrared detectors, such discrepancies could become an even more significant concern for NGST and other future missions.

Also potentially of significant concern are delayed effects of radiation such as radioactivation, phosphorescence, and
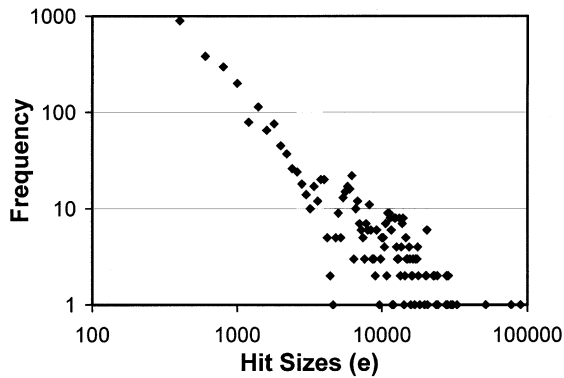
Fig. 10. A composite collection of 16 16-s darkframes taken after NICMOS was reactivated following HST Servicing Mission 3B shows the same general topology seen in the 1998 data.

persistence. Such time-delayed phenomena extend the effects of a radiation event well beyond its duration, making it more difficult to detect and compensate for the resulting delayed contamination. The current study has found little evidence of short-lived radioactivation or other time-dependent effects. Given the limited duration over which the current datasets were gathered, the investigation was not sensitive to longer lived radioactivation. We note, however, that the recent Hubble Servicing mission 3B equipped NICMOS with a new cryocooling system, restoring the instrument's functionality. In the interim, NICMOS has had three additional years of radiation exposure. This opens up the possibility of comparing new NICMOS darkframes to those gathered in 1998 to investigate whether more long-lived radioactivation is evident. To date, the darkframes available from this new operational phase have been too short to reveal a great deal about the radiation response of the detector. Fig. 10 shows a composite of sixteen 16-s data frames taken at different times since NICMOS was recommissioned. Although the composite nature of Fig. 10 makes direct comparison with Fig. 7 difficult, the main characteristics of the 1998 dark frame data are still evident.*

V. CONCLUSION

We have investigated the characteristics of the HST primary and secondary radiation environment by modeling charge collection in NICMOS detectors during dark frame observations. The use of the charge collection model makes it possible to draw general conclusions about the types of particles responsible for a particular event. Using this model, we find the following.

• The model exhibits good qualitative agreement with the data at the low end of the pixel-electron count spectrum, characteristic of short-track segments through multiple pixels and charge sharing via diffusion.

• Agreement is also generally good at the upper end of the spectrum, which is characteristic of proton, alpha, and electron (primary and secondary) strikes to individual and multiple pixels.

• Hits in the upper range of the spectrum tend to be spatially correlated about 50% of the time (compared to 10–20% for smaller hit sizes), possibly indicating that secondary particles and charge sharing among pixels account for the excess of events observed.

• Monte Carlo simulations indicate that up to half of these correlations may be explained by the production of delta rays. Further studies are needed to determine the physics underlying these correlations.

• Significant disagreement with the model is seen for the intermediate range of the spectrum (1500–5000 electron pixel counts).

• Of the potential source terms that may account for this discrepancy, strikes to the Si multiplexer unassociated with strikes to the detector pixel hold out the most promise as an explanation. Range-limited particles incident on the detector from the direction of the Si multiplexer may also contribute. Alternatively, the disagreement may be rectified with changes to the charge collection model, or to the detector model (diffusion length, cell sizes, etc.) assumed in the current study.

• No evidence of delayed source terms in the secondary environment is seen on the time scales (tens of minutes) to which the current study is sensitive.

The recent resurrection of NICMOS after Servicing Mission 3B presents opportunities to further investigate the effects of the primary and secondary radiation environment on infrared detectors. In particular, NICMOS has now had several years of additional radiation exposure, allowing an opportunity to look for evidence of radioactivation on longer timescales. In addition, calibration procedures have been improved for the detector, which may allow investigations of radiation effects at even lower levels of ionization.

REFERENCES

[1] J. C. Pickel, "Novel devices and sensors," in *Proc. IEEE Nuclear and Space Radiation Effects Conf. Short Course Notes*, July 1993, p. IV-1.

[2] T. Boeker, J. Bacinski, L. Bergeron, D. Calzetti, M. Jones, D. Gilmore, S. Holfeltz, B. Monroe, A. Nota, M. Sosey, G. Schneider, E. O'Neil, P. Hubbard, A. Ferro, I. Barg, and E. Stobie, "Properties of PACE-I HgCdTe detectors in space: The NICMOS warm-up monitoring program," *Publications Astron. Soc. Pacific*, vol. 113, July 2001.

[3] P. Agnese, J. J. Engelmann, and P. Mottier, "Results of radiation tests performed on the ISOCAM infrared detector array," *IEEE Trans. Nucl. Sci.*, vol. 38, Aug. 1991.

[4] A. Claret, H. Dzitko, and J. J. Engelmann, "Transient particle effects on the ISOCAM instrument on-board the infrared space observatory," *IEEE Trans. Nucl. Sci.*, vol. 49, p. 1511, Dec. 1999.

[5] D. Calzetti and C. Skinner, "Cosmic rays on NICMOS: Results from thermal vacuum data," Tech. Rep. NICMOS-019, Space Telescope Sci. Inst. (STScI), Baltimore, MD, 1996.

[6] C. J. Skinner and L. Bergeron, "Characteristics of NICMOS detector dark observations," Tech. Rep. NICMOS-97-026, Space Telescope Sci. Inst. (STScI), Baltimore, MD, 1997.

[7] J. C. Pickel, R. A. Reed, R. Ladbury, B. Rauscher, P. W. Marshall, T. M. Jordan, B. Fodness, and G. Gee, "Radiation-induced charge collection in detector arrays," *IEEE Trans. Nucl. Sci.*, vol. 49, pp. 2822–2829, Dec. 2002.

[8] A. Schultz *et al.*, Ed., *Near Infrared Camera and Multi-Object Spectrometer Instrument Handbook for Cycle 11*. Baltimore, MD: Space Telescope Sci. Inst. (STScI), 2001, vol. 4.1.

[9] K. LaBel, P. W. Marshall, C. J. Marshall, M. D'Ordine, M. Carts, G. Lum, H. S. Kim, C. M. Seidleck, T. Powell, R. Abbott, J. Barth, and E. G. Stassinopoulos, "Proton-induced transients in optocouplers: In-flight anomalies, ground irradiation test, mitigation and implications," *IEEE Trans. Nucl. Sci.*, vol. 44, p. 1885, Dec. 1997.

[10] D. Calzetti, "Cosmic rays on NICMOS: Results from on-orbit data," Tech. Rep. NICMOS-022, Space Telescope Sci. Inst. (STScI), Baltimore, MD, June 1997.

[11] S. Kirkpatrick, "Modeling diffusion and collection of charge from ionizing radiation in silicon devices," *IEEE Trans. Electron Devices*, vol. ED-26, p. 1742, 1979.

[12] T. M. Jordan, "An adjoint charged particle transport method," *IEEE Trans. Nucl. Sci.*, vol. 23, p. 1857, Dec. 1976.